

Research papers

Spatial correlation analysis between hydraulic conductivity and specific storage in a heterogeneous sandbox by hydraulic tomography

Liqun Jiang ^a, Ronglin Sun ^{a,*}, Wei Xiao ^a, Xing Liang ^a, Tian-Chyi Jim Yeh ^b^a School of Environmental Studies, China University of Geosciences, Wuhan 430078, China^b Department of Hydrology and Atmospheric Sciences, University of Arizona, Tucson, AZ, USA

ARTICLE INFO

This manuscript was handled by C. Corradini, Editor-in-Chief, with the assistance of Yongjun Jiang, Associate Editor

Keywords:

Hydraulic tomography
Hydraulic conductivity
Specific storage
Spatial correlation
Laboratory sandbox

ABSTRACT

Hydraulic conductivity (K) and specific storage (S_s) are closely related to porosity, the compressibility of aquifer skeleton, connectivity of pores, sorting of the grains, and many others. These well-known relationships promote the investigation of the correlation between spatially varying K and S_s values and their sensitivity to the overlying materials stresses in heterogeneous aquifers. However, the costs of the field experiments for this investigation limit us to a laboratory heterogeneous sandbox aquifer. Before the laboratory experiments, we conducted numerical experiments to verify our tools and approaches. Specifically, we tested the ability of the recently developed hydraulic tomography (HT) for mapping K and S_s fields in two cases. One case in which S_s field was correlated with the K field, and the other was uncorrelated. With the assurance of the ability of our approaches, the laboratory experiments mimicking the numerical ones followed. Accurate drawdown predictions of different flow events in the laboratory experiments further guarantee the reliability of the estimated detailed K and S_s fields. The estimated K and S_s fields reveal that the S_s field's variability is much less significant than K and has much longer correlation scales. Further, the K distribution is closely related to the distribution of sand grain sizes in the sandbox, while S_s is not. Moreover, S_s estimates show a decreasing trend with depth. This trend does not exist in K estimates, indicating that S_s is highly sensitive to overburden stresses and K is not. Lastly, there is no clear spatial correlation between K and S_s , and the variability of S_s is critical in predicting the transient behavior of groundwater flow.

1. Introduction

Hydraulic conductivity (K) and specific storage (S_s) constitute crucial aspects of predicting groundwater flow and contaminants transport for preventing geohazards and protection and management of groundwater resources (e.g., Eramian et al., 1999; Soueid Ahmed et al., 2014; Mao et al., 2018). Notably, the variation of K strongly controls the distributions of contaminants in porous media (e.g., Dagan, 1986; Gelhar, 1986), and the accurate knowledge of S_s is essential for understanding transient groundwater flow and solute transport (e.g., Kuang et al., 2020). It is a critical factor for estimating the capacity of groundwater reservoirs during climate change crises.

Many have focused on the characterization of K variability but less on the variability of S_s (e.g., Cardiff et al., 2012; Hochstetler et al., 2016), let alone the spatial correlation between K and S_s , and the effects of overlying materials stresses on K and S_s in heterogeneous aquifers. Previous numerical studies on K and S assumed that either the S_s

heterogeneity correlated (e.g., Daranond et al., 2020; Zhao and Illman, 2021) or uncorrelated with the K heterogeneity (e.g., Xiang et al., 2009; Hu et al., 2011). They also ignored the impacts of overlying materials stresses. Studies have reported that S_s decreased with increasing overlying materials stresses and decreased with depth (e.g., Terzaghi and Peck, 1967; Sharp and Domenico, 1976; Beavan et al., 1991; Contoux et al., 2013) but not in laboratory-scale sandboxes.

Few have studied the spatial correlation between K and S_s in heterogeneous aquifers. Kuang et al. (2020) collected many K and S_s values from different field sites, covering many aquifer materials, including unconsolidated deposits and rocks. They concluded no clear spatial correlation between K and S_s for all the data but a positive trend for sandstone, limestone, dolomite, and granite. Based on various traditional analytical solutions, their estimated K and S_s values represent ambiguous averages over a large volume, involving considerable uncertainty. The uncertainty in the spatial correlation between K and S_s in heterogeneous aquifers remains answered.

* Corresponding author.

E-mail addresses: sunronglin@cug.edu.cn, likeoasis@163.com, sunronglin@cug.edu.cn (R. Sun).

Using drawdown-time data from an observation well, the traditional analytical analyses, assuming aquifer homogeneity, yield fictitious homogeneous hydraulic parameters, which vary with the pumping and observation duration and location. Wu et al. (2005) criticized the approach as comparing apples with oranges. In order to accurately describe the aquifer heterogeneity, Gottlieb and Dietrich (1995), and many others proposed the hydraulic tomography (HT) technique analogous to electrical resistivity tomographic surveys. It sequentially perturbs (e.g., injecting, pumping, or slug test) an aquifer at different locations and monitors heads at many observation wells. Yeh and Liu (2000) developed and demonstrated the power of the 3-D HT. Their HT inverse algorithm is an iterative geostatistical technique (Yeh et al., 1996, SLE) that uses a stochastic linear estimator successively to incorporate the nonlinear relationship between hydraulic properties and the steady-state heads and update the conditional covariance. Afterward, Zhu and Yeh (2005) developed a sequential successive linear estimator (SSLE) to sequentially interpret transient head data sets from many pumping tests. Xiang et al. (2009) developed a simultaneous successive linear estimator (SimSLE) to simultaneously interpret head data sets from all pumping tests. The robustness of HT in both mapping the K and S_s distributions has been well-documented (e.g., Zhu and Yeh, 2005; Bohling et al., 2007; Liu et al., 2007; Illman et al., 2009; Cardiff et al., 2009; Berg and Illman, 2011; Brauchler et al., 2011, 2013; Castagna et al., 2011; Zha et al., 2015; Wen et al., 2019; Luo et al., 2020; Jiang et al., 2021, and many others).

This study investigates the correlation between spatially varying K and S_s and the sensitivity of the impacts of overlying materials stresses on K and S_s by the HT technique. We achieve this objective in a sandbox aquifer with many pumping tests and monitoring ports to collect sufficient data such that spatially detailed K and S_s distributions can be obtained. We validate these distributions by their ability to produce different flow events. Such elaborate experiments in a field are costly and challenging. While field experiments are the ultimate goal, this laboratory study is a step forward in advancing hydrogeologic science.

This paper briefly introduces SimSLE for HT analysis in section 2. Before sandbox experiments, numerical studies (noise-free) were conducted to ensure the robustness of SimSLE for estimating K and S_s fields of heterogeneous aquifers, where the S_s field is correlated or uncorrelated with the K field. Subsequently, we conducted an HT survey in the laboratory sandbox in section 4 to derive the sandbox aquifer's K and S_s fields. Drawdown predictions of cross-hole pumping tests not used in calibration efforts further warrant the reliability of the estimated fields. The study demonstrates that HT can determine the spatial distribution of K and S_s in a laboratory-scale sandbox. The study also explores the spatial correlation between K and S_s , and the sensitivity of impacts of overlying materials stresses on K and S_s estimates in a laboratory-scale sandbox.

2. Inverse methodology

2.1. Governing flow equation

In this paper, we used the software of VSAFT2 (Variably Saturated Flow and Transport in 2D, Yeh et al., 1993, available at <http://tian.hwr.arizona.edu/downloads> or contact stochasticfusion@gmail.com), to simulate groundwater flow in two-dimensional, saturated, heterogeneous, porous media. The following partial differential equations describe the groundwater flow:

$$\nabla \cdot [K(\mathbf{x}) \nabla H] + Q(\mathbf{x}_p) = S_s(\mathbf{x}) \frac{\partial H}{\partial t} \quad (1)$$

subjected to the boundary and initial conditions:

$$H|_{\Gamma_1} = H_1, [K(\mathbf{x}) \nabla H] \cdot \mathbf{n}|_{\Gamma_2} = q, \text{ and } H|_{t=0} = H_0 \quad (2)$$

In Eq. (1), \mathbf{x} is the spatial coordinate ($\mathbf{x} = \{x, z\}$, [L]), $K(\mathbf{x})$ is the saturated hydraulic conductivity [L/T], H is the total head [L], $Q(\mathbf{x}_p)$ is

the pumping rate (1/T) at the location \mathbf{x}_p , $S_s(\mathbf{x})$ is the specific storage [1/L], and t is time [T]. In Eq. (2), H_1 is the prescribed total head (L) at Dirichlet boundary Γ_1 , \mathbf{n} is a unit vector normal to the Neumann boundary Γ_2 , q is the specific flux (L/T) at Γ_2 , and H_0 represents the initial total head (L) before applying any stress to the aquifer. In this paper, Eqs. (1) and (2) are solved by the software VSAFT2.

2.2. Inversion algorithm

SimSLE, embedded in VSAFT2, basically follows SLE, with the extension that it simultaneously considers the observed head data sets from HT surveys. Both SLE and SimSLE aim to derive the effective parameter field conditioned on available head measurements. They are a geostatistical inverse approach, specified by the mean and covariance of the hydraulic parameters. To avoid obtaining negative values of the estimated parameters, SimSLE conceptualizes parameter's natural logarithm values (i.e., $\ln K(\mathbf{x})$ or $\ln S_s(\mathbf{x}) = \mathbf{f}(\mathbf{x})$) as a spatial stochastic process. Similarly, head (H) is also treated as a spatial stochastic process. These stochastic processes can be expressed as the sum of the unconditional mean and the unconditional perturbation (i.e., $\mathbf{f}(\mathbf{x}) = \langle \mathbf{f}(\mathbf{x}) \rangle + \mathbf{f}'(\mathbf{x})$, and $H(\mathbf{x}) = \langle H(\mathbf{x}) \rangle + h(\mathbf{x})$) (e.g., Zha et al., 2015). The unconditional mean head ($\langle H(\mathbf{x}) \rangle$) is derived from solving the ensemble groundwater flow Eq. (1) with a given unconditional mean ($\langle \mathbf{f}(\mathbf{x}) \rangle$).

Suppose m observed head measurements are collected, expressed as a vector \mathbf{H}^* ($m \times 1$), from an HT survey, consisting of multiple pumping tests. SimSLE then employs a successive linear estimator to derive the conditional effective $\ln K$ perturbation field, $\mathbf{f}_c(\mathbf{x})$, where subscript c denotes conditional. The conditional effective parameter is different from the statistical mean parameter because it produces the most likely head field honoring the observed heads and conforming to the governing Equation, given the observed data (e.g., Gao et al., 2021). The successive linear estimator (SLE) is in Eq. (3).

$$\hat{\mathbf{f}}_c^{(r+1)} = \hat{\mathbf{f}}_c^{(r)} + \boldsymbol{\omega}^{(r)T} [\mathbf{H}^* - \mathbf{H}^{(r)}] \quad (3)$$

In Eq. (3), $\hat{\mathbf{f}}_c^{(r)}$ represents the estimate of $\langle \mathbf{f}(\mathbf{x}) \rangle_c$, given the observed data set (conditioning denoted by the subscript c), r is the iteration index. When $r = 0$, the K and S_s estimates start from an initial guess K and S_s field (unconditional mean K and S_s , in general). Afterward, the estimate of the conditional mean $\langle \mathbf{f}(\mathbf{x}) \rangle_c$ is successively improved by the weighted difference between \mathbf{H}^* (the observed head data) and the vector $\mathbf{H}^{(r)}$ (the simulated head data). These simulated head data are obtained from the conditional mean equation (Eq. (1)) with the estimate of the conditional mean $\hat{\mathbf{f}}_c^{(r)}$ at the iteration r .

The coefficient matrix $\boldsymbol{\omega}$ is determined by solving the following Equation:

$$[\mathbf{R}_{hh}^{(r)} + \mathbf{Q}_h + \theta \text{diag}(\mathbf{R}_{hh}^{(r)})] \boldsymbol{\omega}^{(r)} = \mathbf{R}_{hf}^{(r)} \quad (4)$$

$\mathbf{R}_{hh}^{(r)}$ is the unconditional head covariance matrix at $r = 0$, and is the conditional covariance at $r > 0$. Similarly, $\mathbf{R}_{hf}^{(r)}$ is the unconditional cross-covariance matrix between parameter and head measurement at $r = 0$, and is the conditional one at $r > 0$. θ is a stability multiplier and $\text{diag}(\mathbf{R}_{hh}^{(r)})$ is a stability matrix, which is the diagonal elements of the $\mathbf{R}_{hh}^{(r)}$ matrix. \mathbf{Q}_h is a diagonal matrix ($m \times 1$) of variances of measurement errors if specified (e.g., Jiang et al., 2021).

In Eq. (4), the covariance matrix $\mathbf{R}_{hh}^{(r)}$ and cross-covariance $\mathbf{R}_{hf}^{(r)}$ matrix are approximated by using first-order analysis: $\mathbf{R}_{hh}^{(r)} = \mathbf{J}_{hf}^{(r)} \mathbf{R}_{ff}^{(r)} \mathbf{J}_{hf}^{(r)T}$ and $\mathbf{R}_{hf}^{(r)} = \mathbf{J}_{hf}^{(r)} \mathbf{R}_{ff}^{(r)}$ respectively, where $\mathbf{J}_{hf}^{(r)}$ is the sensitivity (or Jacobian) matrix for the observed head data location to the parameter everywhere in the domain, evaluated using $\hat{\mathbf{f}}_c^{(r)}$ at the r th iteration (e.g., Tso et al., 2016). At $r = 0$, the covariance matrix for parameters $\mathbf{R}_{hh}^{(r)}$ is unconditional and is essentially the spatial covariance matrix \mathbf{R}_{ff} . It can

be obtained using a user-specified covariance function. In the subsequent iterations, the covariance matrices become conditional (or residual) covariance given the observations and are updated to reflect the successive improvements in the estimates:

$$\mathbf{R}_{ff}^{(r+1)} = \mathbf{R}_{ff}^{(r)} - \mathbf{\omega}^{(r)T} \mathbf{R}_{hf}^{(r)} \quad (5)$$

Mathematically, this updating procedure is similar to the Kalman filter algorithm (e.g., Schöniger et al., 2012) as the new information is included. This approach is unique to other inverse approaches: it expedites the convergence of the solutions. The above steps are repeated until the two convergence criteria are satisfied. 1) the change in variances of the $\ln K$ and $\ln S_s$ estimates between the current and the previous iteration change is less than a user-specified value. 2) The change in simulated heads between successive iterations is smaller than a specified value. Once one of the two criteria is met, we consider the estimates optimal and terminate the iteration (e.g., Jiang et al., 2021).

2.3. Performance metrics

The best way to evaluate the reliability of K and S_s estimates is to compare the estimates with the true parameter values by scatterplots, and this comparison is very easy for numerical studies. However, true parameter values are unknown in the physical sandbox and field, and thus the scatter plot is impossible. Alternatively, the K and S_s estimates can be assessed by validation. We assess the reliability of K and S_s estimates by their abilities to predict drawdown of cross-hole pumping tests not used in calibration efforts.

Following this logic, in sandbox studies, we choose the measured drawdown data at ten different times (0.1, 0.3, 0.5, 0.7, 1.0, 1.5, 2.0, 2.5, 3.0, and 10 s), covering early, intermediate, and late time stages, generated by the pumping tests not used to estimate K and S_s fields for model validation purpose. Afterward, we use the estimated K and S_s fields to simulate the groundwater flow in forward modeling for obtaining predicted drawdown data.

The coefficient of determination (R^2), also called the multiple correlation coefficient, is well established in classical regression analysis (Rao, 1973). Its definition as the proportion of variance explained by the regression model (e.g., the linear model), makes it useful as a measure of success in predicting the dependent variable from the independent variables (Nagelkerke, 1991). Thus, R^2 is a statistical measurement that assesses how strong the relationship is between two variables. R^2 can be utilized to evaluate the similarity between the predicted and measured drawdowns in sandbox studies (or the reference and estimated $\ln K$ ($\ln S_s$) values in numerical studies). A high R^2 value means that the predicted (or estimated) and measured (or reference) data are highly correlated. A linear model is used to fit the pairs of scatterplots. The fitted linear model reports the slope and intercept of the best-fit line. Also, the mean absolute error (MAE) and the mean square error (MSE) are also calculated as metrics. MAE and MSE norms are defined as:

$$MAE = \frac{1}{N} \sum_{i=1}^N |x_i - y_i| \quad (6)$$

$$MSE = \frac{1}{N} \sum_{i=1}^N (x_i - y_i)^2 \quad (7)$$

In Eqs. (6) and (7), N is the total number of the drawdowns or hydraulic parameters, i indicates the data number, x_i and y_i represent the predicted and measured drawdowns (or the estimated and reference parameters), respectively. Both MAE and MSE norms express how far the predicted drawdowns (or estimated parameters) are from the measured drawdowns (or reference parameters).

3. Numerical experiment

3.1. Experimental design

The numerical experiment considered a two-dimensional, saturated, and heterogeneous aquifer (180 cm in the x-axis, 90 cm in the z-axis, Fig. 1a). For the HT analysis, the aquifer domain was discretized into 36 vertical and 36 horizontal elements (a total of 1296 elements and 1369 nodes) with a dimension of 5 cm (x-axis) \times 2.5 cm (z-axis). The aquifer's left, right, and top boundaries were assigned the constant-head boundaries of 95 cm, while the bottom, front, and back faces were impermeable.

This experiment considered two types of heterogeneous K and S_s fields (i.e., Cases 1 and 2) to investigate HT's ability to detect the spatial relationship between K and S_s . **Case 1** represents perfectly correlated heterogeneous K and S_s fields, while **Case 2** the completely independent fields. The two cases have the same K field but different S_s fields. The K field has a mean K of 0.233 cm/s, a variance $\ln K$ of 1.0, and a correlation scale of 90 cm in the x-direction and 10 cm in the z-direction using an exponential covariance function. On the other hand, the two S_s fields have a mean S_s of 0.0005 /cm, a variance $\ln S_s$ of 0.2, and a correlation scale of 90 cm in x-axis/10 cm in z-axis with an exponential covariance function.

Using a Fast Fourier Transform (FFT) random field generator (Gutjahr, 1989), we generated spatially varying K and S_s values for the 1296 elements. The random seed used to generate the K field was used to create the S_s field perfectly correlated with the K field (Case 1) and independent (Case 2) otherwise.

The generated K field for the two cases is shown in Fig. 1a, while the S_s field perfectly correlated with the K field (Case 1) is plotted in Fig. 1b. At the same time, the uncorrelated S_s field (Case 2) is illustrated in Fig. 1c. As indicated in Fig. 1a and 1b, the perfectly correlated S_s field has an identical pattern to the K field, although the values are different. Conversely, the uncorrelated S_s field (Fig. 1c) has an entirely different spatial pattern from that of the K field (Fig. 1a). These fields are our reference (or actual) fields for numerical experiments.

After generating the reference K and S_s fields, five columns of monitoring ports were installed (the solid black circles shown in Fig. 1a) — each column has eight ports. Subsequently, we conducted an HT survey, which involved a series of cross-hole pumping tests at all 40 ports with a constant pumping rate until steady-state conditions. Head measurements were collected at other 39 monitoring ports, excluding the pumping port, during each pumping test. In the end, we have 40×39 drawdown-time curves for each case.

3.2. Head data selection

Fig. 2 illustrates our data-time sampling strategy following Sun et al. (2013) for transient HT analysis. Head values at five selected early and late times (A1, A2, A3, A4, and A5) were extracted from each drawdown curve. The late time or steady-state head (A5) has the highest correlation with $\ln K$ heterogeneity over a large aquifer region. The head at the early time (A1, A2, A3, and A4) around the time " t_0 " has the highest sensitivity with $\ln S_s$ heterogeneity over the aquifer areas between the pumping and the monitoring port. The time " t_0 " is when the drawdown from the straight-line portion of an observed drawdown-log time plot becomes zero (Cooper and Jacob, 1946). We first used the steady-state heads and HT analysis (SSHT) to estimate the K field based on Sun's suggestion. The estimated K field is treated as a known, and transient HT analysis (THT) then estimates the S_s field. Following Mao et al. (2013) and Wen et al. (2019), we used heads at four early times to estimate S_s and avoid noise issues. Twenty pumping tests (from ports 10, 11, 12, 13, 14, 15, 16, 18, 19, 20, 21, 22, 23, 26, 27, 28, 29, 30, 31, and 32, Fig. 3a) were chosen for HT analysis.

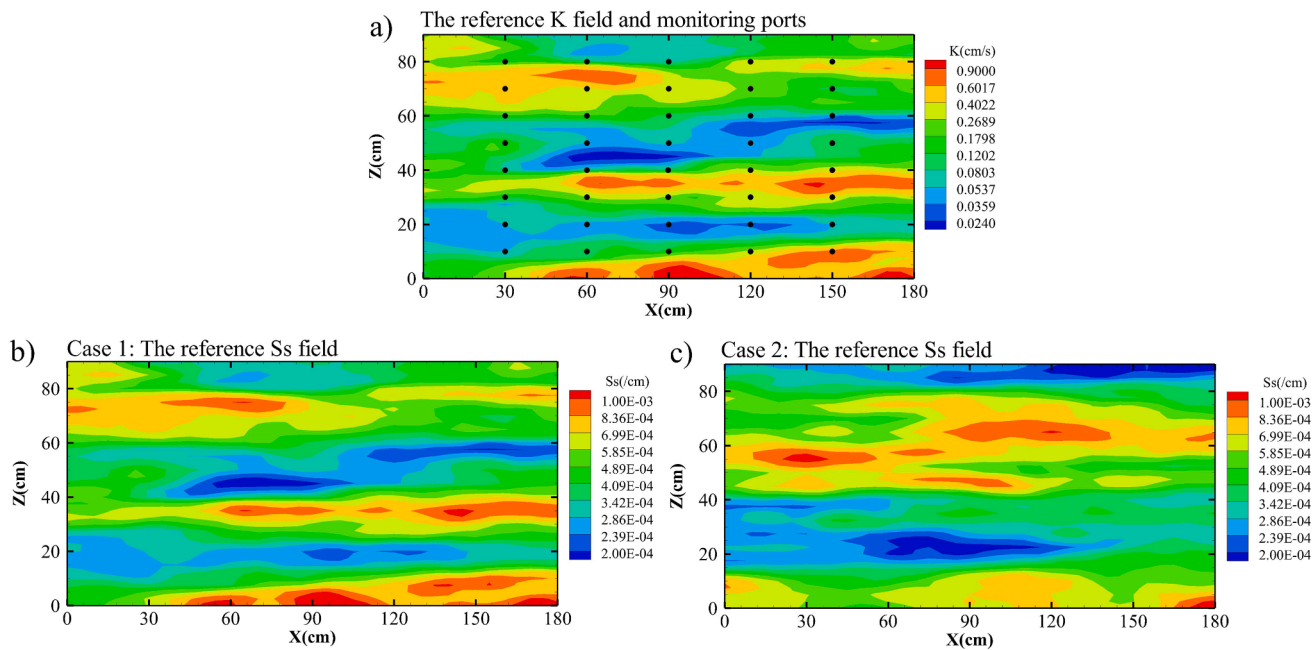


Fig. 1. a) The reference K field and monitoring ports. Black solid circles show the location of monitoring ports. b) Case 1: The reference S_s field which is correlated with the reference K field; and c) Case 2: The reference S_s field which is uncorrelated with the reference K field.

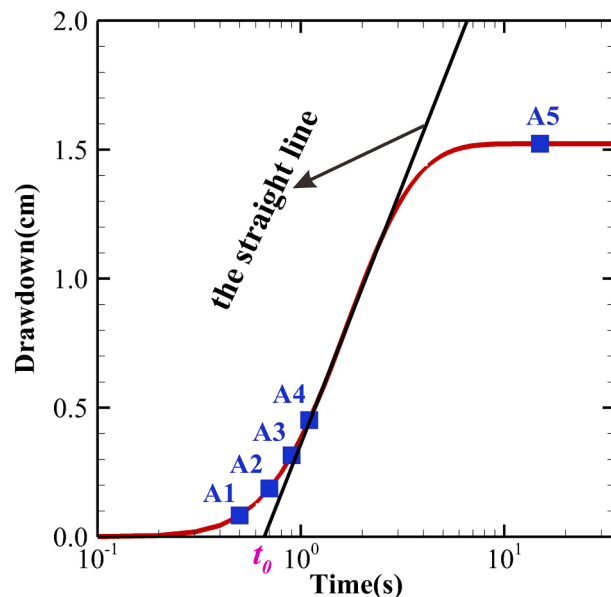


Fig. 2. Concept plot of the data selection scenario for HT technique in this study.

3.3. Results of numerical studies

The estimated K field is displayed in Fig. 3b, while the estimated S_s field in Case 1 is in Fig. 3c, and that in Case 2 is in Fig. 3d. Comparing Fig. 3b with Fig. 1a reveals that SSHT with SimSLE yields a K distribution closely resembling the actual K field. Likewise, THT with SimSLE also yields a S_s field mimicking the actual one (comparing Fig. 3c with Fig. 1b, and Fig. 3d with Fig. 1c). Table S1 in the Supplementary material section compares the spatial statistics of the estimated and actual fields for the two cases. They are in close agreement, but the estimated statistics are slightly smaller than the true.

The scatterplot of the reference versus estimated K field is shown in Fig. 4a, while the reference versus estimated S_s field in Case 1 is in

Fig. 4b, and Case 2 in Fig. 4c. All figures show the data are scattering around the 1:1 line, with R^2 values (0.797, 0.758, and 0.759, respectively), MAE values (0.360, 0.173, and 0.174, respectively), and MSE values (0.210, 0.049, and 0.049, respectively) since the limited number of ports makes inverse problem not well-defined. Nevertheless, SimSLE yields accurate estimates of the true K and S_s fields in the two cases. These estimates were then analyzed for the spatial correlation between K and S_s (see Figure S1 in the Supplementary Material section). These numerical experiments confirm that SimSLE is a robust inverse algorithm and is ready for sandbox experiments.

4. Sandbox experiment

4.1. Sandbox settings

A laboratory sandbox was constructed (Fig. 5a) (Xu et al., 2019), mimicking the numerical experiment, but filled with predetermined 19 layers of five types of sands with different grain sizes and permeability (Fig. 5b). Table 1 tabulates the grain size, saturated hydraulic conductivity, and porosity for five materials before filling the sandbox (Jiang et al., 2021). Identical to the numerical experiment, 40 partly-penetrating monitoring ports were installed on the backside of the sandbox after the sandbox was packed with sands. These monitoring ports could be connected to either a pressure transducer as a monitoring port or a peristaltic pump as a pumping or injection port via the silicone tube (Fig. 5c).

4.2. HT surveys

Cross-hole pumping tests for HT surveys at all the 40 monitoring ports were then undertaken. A data logger recorded the head changes every 0.1 s at the other 39 ports during the pumping test at a pumping port until the head changes stabilized. Afterward, we turned off the pump and allowed the heads to rebound to the initial head of 95 cm. We repeated the cross-hole pumping test by moving the pump to another port until all 40 ports were pumped. The constant pumping rate at ports 11, 19, 23, 31 was $Q = 9.168 \text{ ml/s}$, and $Q = 18.336 \text{ ml/s}$ at the other 36 ports to induce noticeable drawdown due to differences in aquifer hydraulic properties.

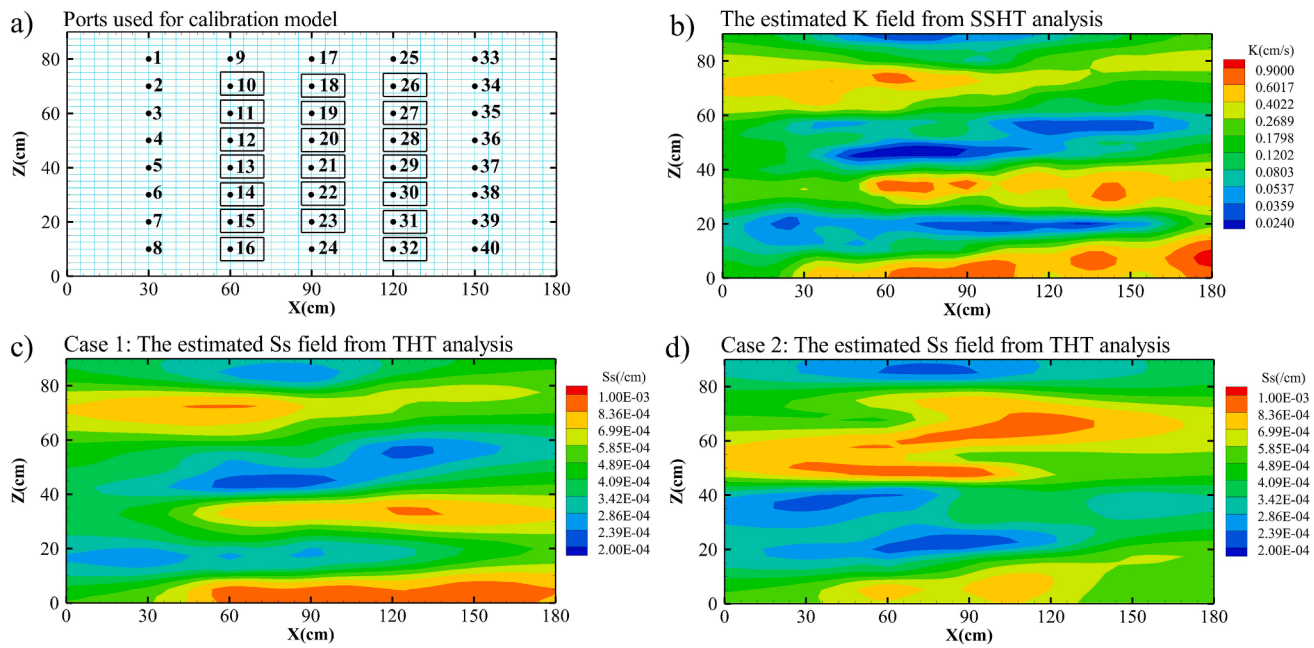


Fig. 3. a) Locations of monitoring ports used for calibration model. 20 black rectangles indicate the 20 ports pumped and the head data used for estimating K and S_s fields. Estimated parameter fields: b) The estimated K field; and c) The estimated S_s field in Case 1; and d) The estimated S_s field in Case 2.

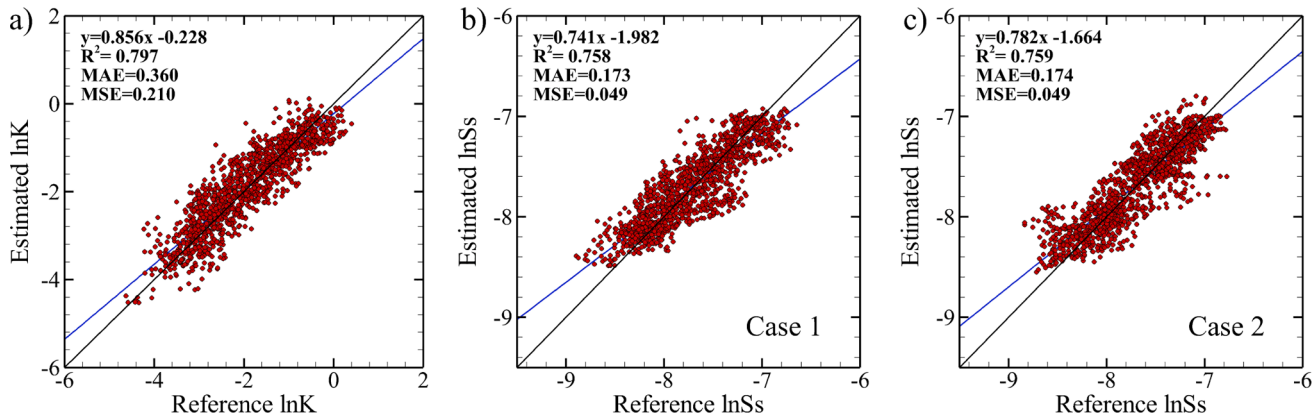


Fig. 4. Scatterplots of a) the reference versus estimated $\ln K$ values; b) the reference versus estimated $\ln S_s$ values in Case 1; and c) the reference versus estimated $\ln S_s$ values in Case 2. The black solid line is a 1:1 line indicating a perfect match. The blue line is the best fit.

Estimating parameters in the sandbox experiment used the same twenty pumping tests and time sampling strategy of the numerical experiment. On the other hand, validation utilized data generated from pumping tests at ports 4, 5, 24, 36, and 37 (Fig. 5b).

4.3. Results and validation

4.3.1. Estimated K and S_s fields from HT and permeameter measurements

Fig. 6a is a sketch of the 19 layers in the sandbox aquifer, based on a visual examination of different grain size distributions and their K values obtained from permeameter experiments (Table 1). The SSHT estimated K field is illustrated in Fig. 6b, and the THT estimated S_s field is in Fig. 6c.

Comparing Figs. 6b with 6a highlights that SSHT estimates are in good agreement with the visual one at layers 1, 4, 5, 8, 9, 12, 14, 15, 16, and 19, capturing the layer structure of the sandbox aquifer. The limited number of ports, estimation, and head measurement errors in SSHT may be the causes of some discrepancies in detail.

Figs. S2 through S6 in the supplementary material section show the frequency distributions of SSHT K estimates within the layers

constructed by each of the five materials. Color vertical bars are the frequency distributions for the layers, and the vertical red dashed line represents the permeameter measured K of the material used to pack the layers. These figures reveal different spread patterns of the estimated K values in different layers, even though they were packed with the same material. Further, their mean values are different from the permeameter measured K . Thus, the K distribution in Fig. 6a, based on visual examination and the permeameter measured K for each material, may not represent the actual K distribution in each layer in the sandbox. The effects of such discrepancies are addressed in the validation section (4.3.4).

Despite the difference in detailed estimated K values and the permeameter measured K for each material, the layers' structure due to the grain size difference is apparent in Fig. 6a. As such, K heterogeneity is closely related to the grain size of sands. Examination of Table 1 reveals that these measured K values from permeameter experiments increase with sand grain sizes. A similar K -grain size trend also exists in Fig. 6b if we compare the layer number and the estimated K value to those in the Table 1. The estimated S_s field in Fig. 6c does not exhibit a clear layering structure as in Fig. 6b, nor does it show any relationship with grain size.

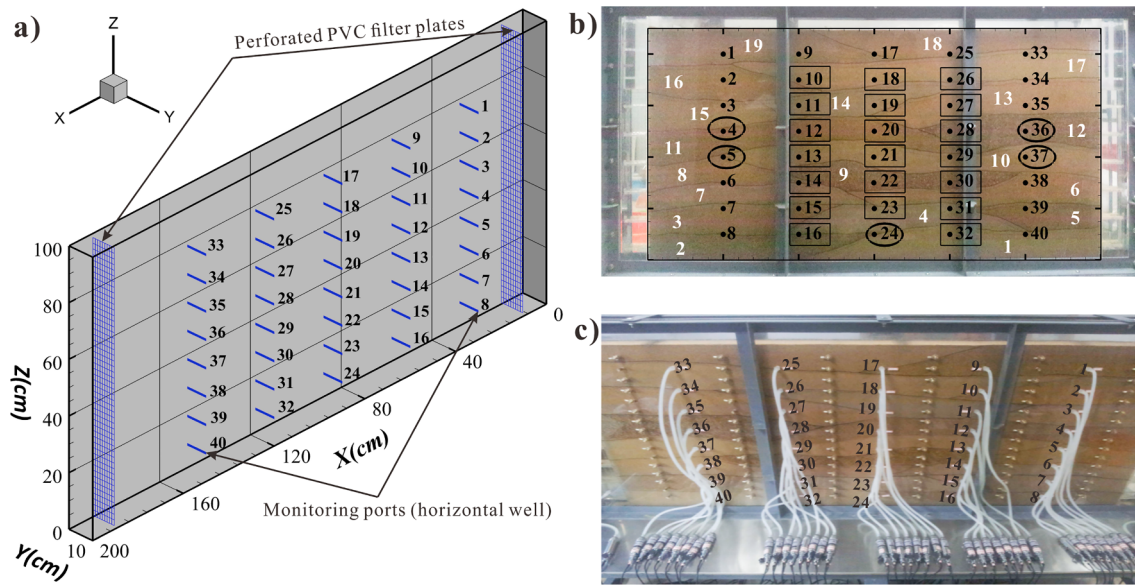


Fig. 5. a) Conceptual graph of the sandbox. The blue lines represent monitoring ports (horizontal wells in y orientation) for HT technique, and black numbers next to blue lines indicate monitoring port numbers. b) The front-side photograph of the lab sandbox. White numbers indicate numbers of 19 sand layers. 20 black rectangles indicate the 20 ports pumped and heads used to estimate K and S_s fields, and 5 black ellipses indicate the 5 ports pumped and heads used for validation. c) The backside photograph of the lab sandbox.

Table 1

The hydraulic parameters of the five materials for the laboratory sandbox experiments aquifer.

Layer number	Grain size (mm)	K (cm/s) permeameter	Porosity
Material 1: layers 4, 14	0.10–0.25	0.0180	0.3892
Material 2: layers 1, 7, 10, 15, 17	0.25–0.40	0.0788	0.3770
Material 3: layers 3, 6, 8, 13, 16, 18	0.30–0.60	0.1395	0.3712
Material 4: layers 2, 5, 11, 19	0.60–1.00	0.3352	0.3737
Material 5: layers 9, 12	1.00–4.00	0.8527	0.3788

Note: Due to the effect of sedimentation and packing, these measured K values before packing the sandbox cannot accurately reflect the true K distribution of the sandbox aquifer (Jiang et al., 2021).

Zhao and Illman (2021) reported a similar finding.

4.3.2. Statistical properties of K and S_s estimates

Few studies have reported the frequency distribution of S_s over the past. Therefore, we present the histograms of $\ln K$ and $\ln S_s$ estimates in Fig. 7, which exhibit general normal distributions and show that the number of extremum (low-zone and high-zone values) is small.

Table 2 tabulates their spatial statistics, including the mean, variances, coefficient of variation (i.e., CoV), and correlation scale (exponential model) of $\ln K$ and $\ln S_s$ estimates. The CoV corroborates that S_s heterogeneity is much lower than K heterogeneity.

Yeh et al. (2015) articulated that correlation scales in the covariance function of the parameter represent the average length, thickness, and width of the dominant heterogeneities in a formation. Table 2 shows that the correlation scales of the estimated K values agree with the average dimension of layers of different grain sizes. S_s estimates in Fig. 6c, however, show ambiguous layering. According to Table 2, the correlation scales for $\ln S_s$ are longer than $\ln K$, indicating that S_s is less dependent on the grain size, which is the factor creating the layer structure.

4.3.3. Impact of ignoring S_s heterogeneity on predicting groundwater flow

Many HT analyses ignore the variability of S_s , attributing to

difficulties in estimating it (e.g., Tiedeman and Barrash, 2020). They often justify it by its smaller variability than K , as supported by our laboratory experiments, and its insignificant impacts (e.g., Cardiff et al., 2012; Hochstetler et al., 2016). This paper shows that SimSLE is quite capable of estimating S_s . The need to investigate the validity of S_s estimates and the impact of the heterogeneity of S_s estimates on predicting transient groundwater flow becomes imperative. For this purpose, we compare simulated aquifer responses using the detailed K field with the arithmetic mean of S_s estimates ($1.50 \times 10^{-4} / \text{cm}$) and with the detailed S_s estimates in the validation next.

4.3.4. Validation of the estimated parameters

Fig. 8a and b show the measured versus predicted drawdowns recorded at ten times at each observation port during the five pumping tests. The predicted drawdowns in Fig. 8a were simulated using K estimates from SSHT, and S_s estimates from THT. In contrast, those based on K estimates from SSHT with the arithmetic mean of S_s estimates from THT are in Fig. 8b. Examining these two figures reveals that R^2 decreases from 0.977 to 0.924. Likewise, MAE increases from 0.080 to 0.151, and MSE increases from 0.021 to 0.076, indicating that incorrectly treating the heterogeneous S_s field as a homogeneous one leads to less desirable predicted drawdown distributions.

The continuous measured and predicted drawdown-time curves at all 39 selected monitoring ports during the validation using pumping port 24 are plotted in Fig. 9 (Figs. S7 and S8 in the supplementary material section are for ports 5 and 37, respectively). In Fig. 9 and those in the supplement, the solid black lines indicate the predicted drawdown-time curves based on K estimates from SSHT and S_s estimates from THT. The solid green lines represent the predicted drawdown-time curves based on K estimates from SSHT and the mean of S_s estimates from THT. The red circles are the measured drawdown data.

The overall match of the measured and the predicted drawdown-time curves using HT estimates are more satisfactory than those ignoring the heterogeneity of S_s . The disparities in drawdown-time curves are apparent. Deviations of HT estimates' predictions from the measured curves are observed at ports 1 and 33, near the constant-head boundary at the top of the sandbox aquifer, likewise at ports 8, 16, 32, and 40 located near the impermeable boundary at the bottom. We found that the overall match was poor near the pumping wells. Gelhar (1993)

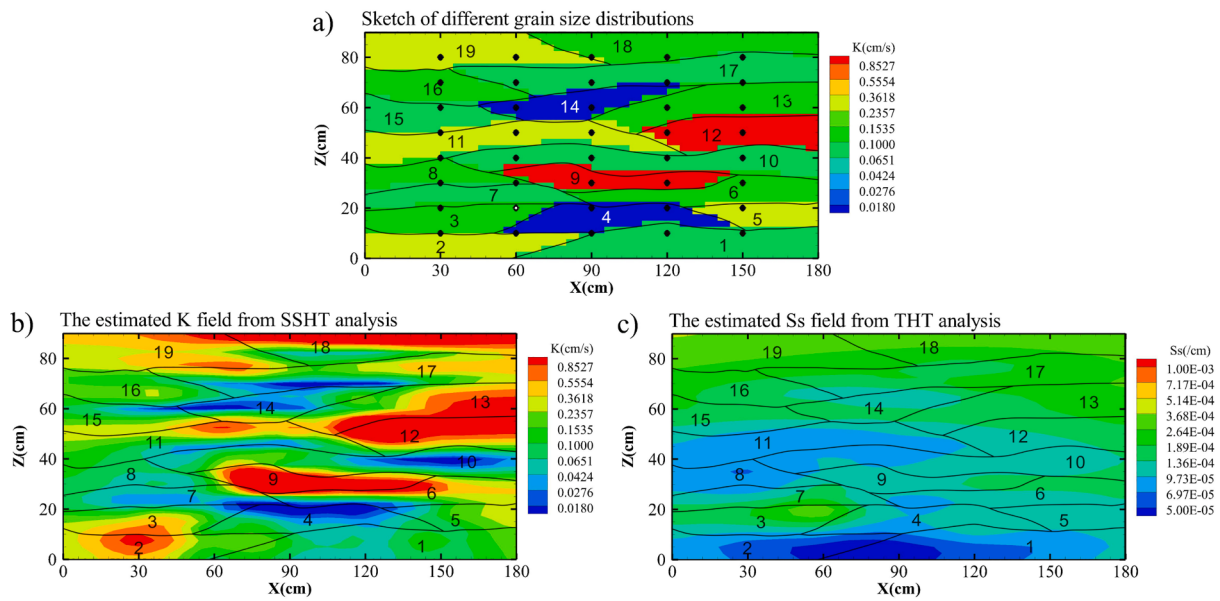


Fig. 6. a) Sketch of different grain size distributions; b) the estimated K field from SSHT analysis; and c) the estimated S_s field from THT analysis. Black lines indicate the shape of each layer.

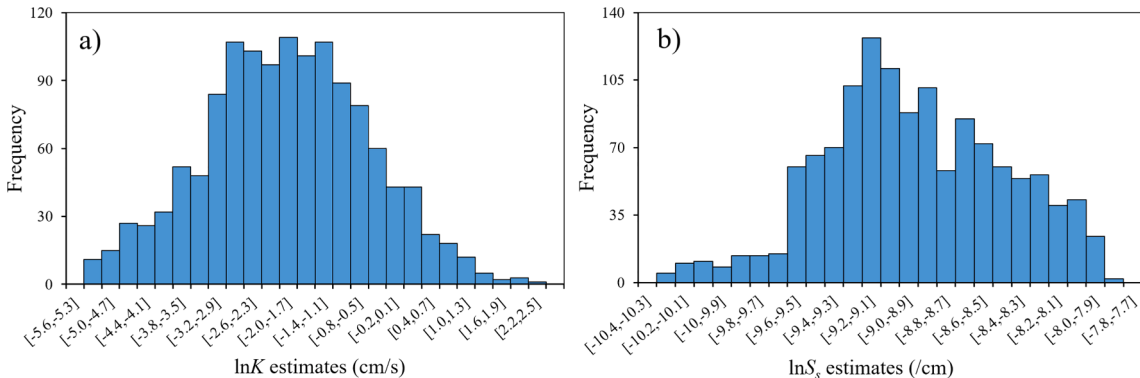


Fig. 7. Frequency distributions of a) $\ln K$ estimates; and b) $\ln S_s$ estimates.

Table 2

Comparison of statistical properties of K and S_s estimates obtained from HT in sandbox studies.

Parameter	Mean	Variance	Coefficient of Variation (CoV)	Correlation scale (cm)	
				λ_x	λ_z
lnK from SSHT	-1.88	1.90	5.38×10^{-1}	41.2	11.6
lnS _s from THT	-8.92	0.24	2.97×10^{-3}	64.8	26.5

theoretically showed that head variances increase with large head gradients with a given heterogeneity. Because the gradient is large near the pumping wells, a slight parameter estimation error leads to a large discrepancy in head prediction. Significant disparities between the measured and predicted drawdowns near the pumping wells are expected. Besides, a steep gradient near the pumping well requires extremely fine grids to simulate the true head correctly. For these reasons, reproducing the heads near the pumping well is difficult. Overall, Figs. 8 and 9 demonstrate that SimSLE yields reliable K and S_s fields of heterogeneous aquifers, and S_s heterogeneity impacts the prediction.

The reliability of SSHT estimated K and the permeameter measured K

for the 19 layers is illustrated in Fig. 10a and b. The scatterplot of the measured and predicted steady heads of the validation experiments using SSHT estimated K is depicted in Fig. 10a, and that using the visualized layering and the permeameter measured K is in Fig. 10b. The former outperforms the latter. As discussed in Section 4.3.1, the permeameter measured K in each layer does not capture the widely spread K values from SSHT, nor do they agree with the mean of K estimates from SSHT. Nonetheless, predicted drawdowns using the visualized layer structures with the permeameter measured K values generally agree with the measured drawdown during the validation.

4.3.5. Changes in K and S_s with depth

Fig. 11a shows the relationship between S_s estimates and depth, and Fig. 11b displays K estimates versus depth. A power-law model (e.g., Bredehoeft et al., 1992; Manning and Ingebritsen, 1999; Ingebritsen and Manning, 2010) nicely describes the S_s -depth data — S_s estimates from THT decrease with depth. However, no such trend exists in K -depth plot (Fig. 11b), suggesting that S_s is sensitive to the overlying material stresses and K is not. Since the grain size appears to be related to the K (Table 1), one may conclude that the grain size in the sandbox does not change with the depth, likely due to the light overburden stress. Previous studies (e.g., Beavan et al., 1991; Contoux et al., 2013) also stated

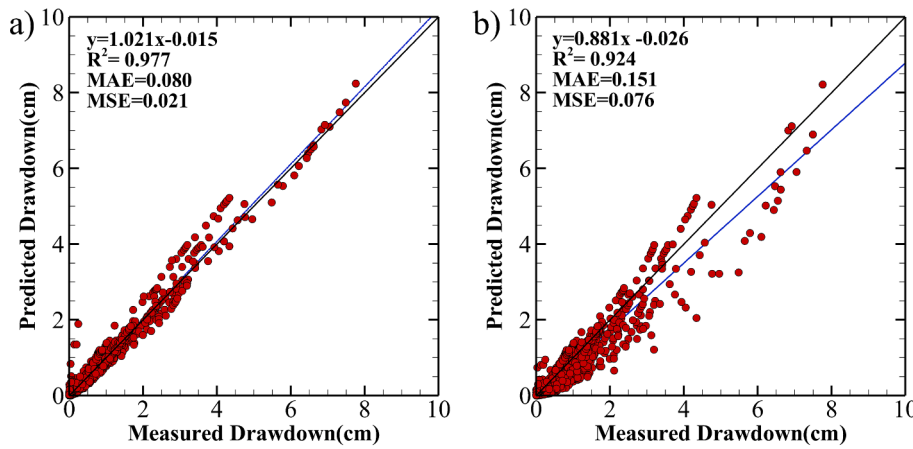


Fig. 8. Validation scatterplots of the measured versus predicted drawdowns from the forward simulation based on the parameter fields: a) K estimates from SSHT and S_s estimates from THT; and b) K estimates from SSHT and arithmetic mean (1.50×10^{-4} /cm) of S_s estimates from THT.

that S_s decreases with depth. [Sepúlveda and Zack \(1990\)](#), using a laboratory experiment, noticed that S_s values throughout the vertical thickness of shallow artesian aquifers varied overburden stresses. [Sepúlveda and Zack \(1991\)](#) reported that K changes due to overburden stress are of a lesser order of magnitude compared with S_s changes.

[Brauchler et al. \(2011, 2013\)](#) analyzed THT field experiments in the aquifer with shallow unconsolidated river sediments to compute diffusivity (D) and S_s tomograms, and found a decrease of S_s estimates with depth. However, [Illman et al. \(2009\)](#) and [Zha et al. \(2015\)](#) analyzed THT field experiments in a fractured granite aquifer to compute K and S_s tomograms. [Berg and Illman \(2011\)](#) used THT in a highly heterogeneous glaciolacustrine aquifer-aquitard system (including sand, sandy gravel, silt, silty clay, and others) to estimate K and S_s tomograms. These investigations did not analyze the relationship between K (S_s) estimates from HT and depth, but their K and S_s tomograms suggested no clear relationship between K (S_s) and depth. Moreover, compaction in different sediments from overlying materials stresses is different. Few investigated the relationship between S_s values in a type of sediment (e.g., only silt) and depth in the field sites with diverse sediments (e.g., sandy gravel, silt, sand, sandy gravel).

4.4. Spatial correlation analysis between K and S_s

Examining Fig. 6b and c reveals that the estimated S_s field has an entirely different spatial pattern from the estimated K field. This observation is substantiated by the scatterplot of $\ln K$ versus $\ln S_s$ estimates in Fig. 12, which shows that the R^2 of 0.069 indicates no clear relationship between K and S_s . Similar findings are available in [Illman et al. \(2009\)](#), [Berg and Illman \(2011\)](#), and [Zha et al. \(2015\)](#). These investigations did not analyze their relationship, but their K and S_s tomograms suggested no clear spatial correlation between K and S_s in heterogeneous aquifers.

5. Discussion

Mathematically, K can be expressed as (e.g., [Bear, 1972](#)).

$$K = k \frac{\rho g}{\mu} \quad (8)$$

In Eq. (8), k represents the intrinsic permeability (L^2), ρ is the water density (M/L^3), g is the acceleration due to gravity (L/T^2), and μ is the dynamic viscosity of a fluid (M/LT). k is often expressed as the Kozeny-Carman equation (e.g., [Bear, 1972](#)).

$$k = \frac{d_m^2}{180} \frac{n^3}{(1-n)^2} \quad (9)$$

In Eq. (9), d_m is mean particle size (L), and n is the porosity (–). This Equation implies that the porosity is independent of the mean grain size, and k is independent of flow characteristics. [Athy \(1930\)](#) noted that the porosity n mainly depends on the size, shape, degree of uniformity of size and shape, and the packing of grains. The porosity in the sand is independent of the size of grains, provided they are of one size and spherical.

A more general and flexible relationship for k and d_m is.

$$k = Nd_m^2 \quad (10)$$

where N is the coefficient that accounts for effects of factors other than the d_m (such as effective porosity for flow, connectivity of pores, and tortuosity of the flow path) ([Bear, 1972](#)).

Notice that both Equations (9) and (10) indicate a quadratic relationship between k and d_m . The relationship between the K and the d_m for the five materials from permeameter measurements (Table 1) is linear, as displayed in Fig. S9a. Meanwhile, Fig. S9b illustrates the mean of the SSHT estimated K values of the layer corresponding to each of the five materials and d_m . In this figure, the SSHT estimated K values in the layers corresponding to a given material were averaged to derive the mean K of that material. These two figures implicate a linear relationship between K and d_m , different from Eqs. (9) and (10). This disparity may be due to only five K , d_m , and n measurements for the materials, and our experiments were not well suitable to test these formulas. Nevertheless, the results of our experiments support that K increases with d_m .

The S_s is the volume of water per volume of a porous medium released from or stored in the porous media per change in the total head, due to expansion of the water or deformation of the grain skeletons (e.g., [Hantush, 1964](#)). S_s has been expressed (e.g., [Cooper, 1966](#); [Van der Kamp and Gale, 1983](#)) as.

$$S_s = \rho g(\alpha + n\beta) \quad (11)$$

In Eq. (11), α represents the compressibility of the aquifer matrix (LT^2/M) resulting from the expansion, restructure, or deformation of the individual rock grains, induced by the change in the surrounding fluid pressure (e.g., [Hall, 1953](#)). Similarly, β is the compressibility of water (LT^2/M) affected by the pressure and temperature (e.g., [Kell, 1975](#)). Eq. (11) shows that the S_s term is closely related to the porosity, compressibility of the aquifer skeleton, and water. In our experiments, the five materials' porosity was measured in the permeameter experiments, but no direct porosity measurements in the sandbox were conducted. The observed changes in S_s estimate with depth (Fig. 11a) may be attributed to the change in α or n or both. However, we cannot make verify this speculation.

Past studies reported that the porosity generally showed a decreasing trend with the depth (e.g., [Chilingarian, 1983](#); [Chen et al., 2020](#)), but the

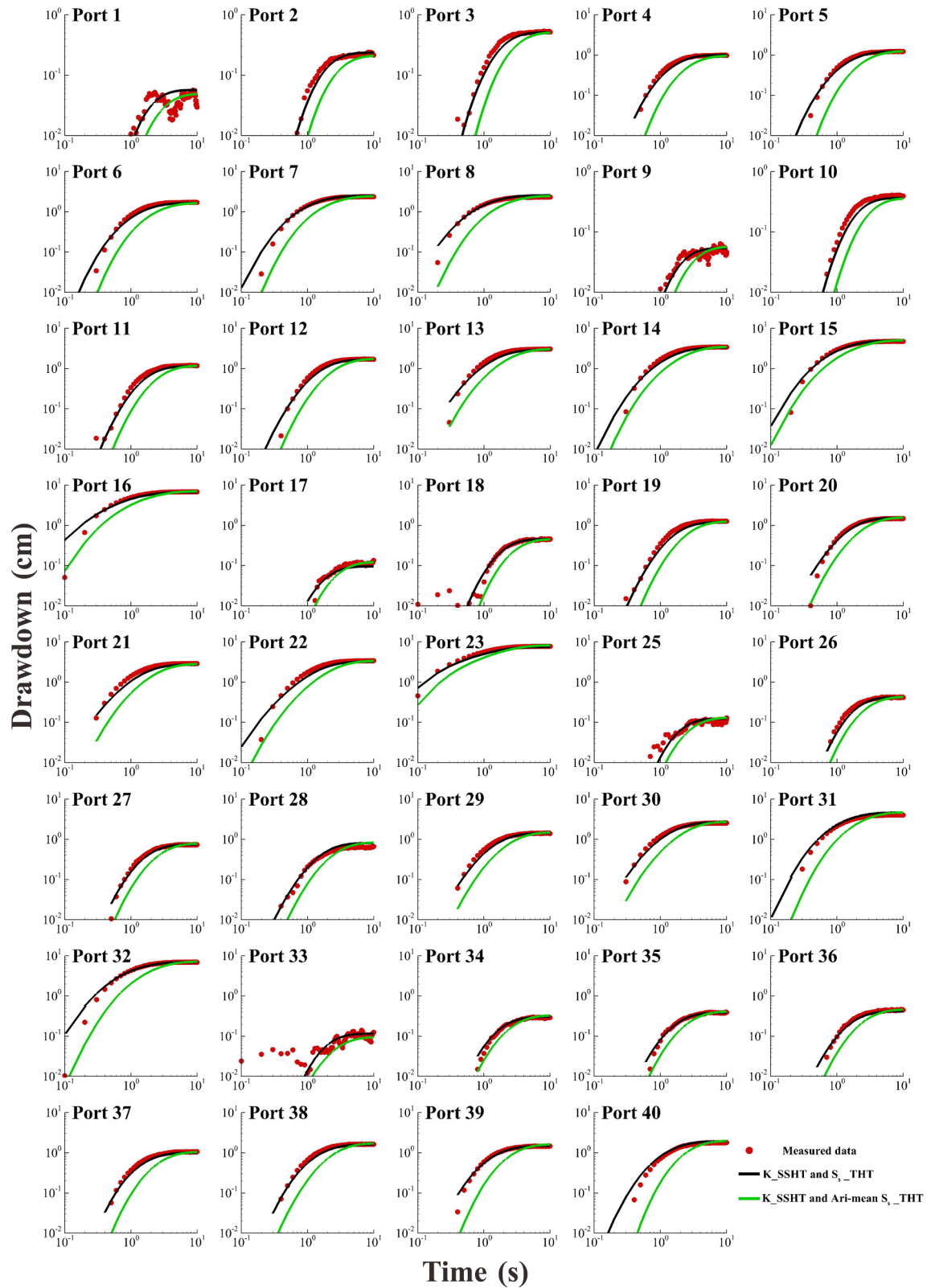


Fig. 9. The measured versus predicted drawdown-time curves at all 39 selected monitoring ports when conducting a cross-hole pumping test at port 24 not used in calibration efforts.

decreasing trend was minimal in shallow aquifers. For example, [Sepúlveda and Zack \(1991\)](#) investigated the effect of overburden stress on S_s and K of artesian aquifers with a depth of 90 m. They showed that the n values decreased from 0.451 to 0.438, from 0.367 to 0.366, from 0.471

to 0.455, from 0.383 to 0.381 in different effective stresses. Then, [Elias and Hajash \(1992\)](#) noted that n decreased steadily under constant nonzero effective stress at 150 °C, but remained essentially constant under identical loading conditions at room temperature in experimental

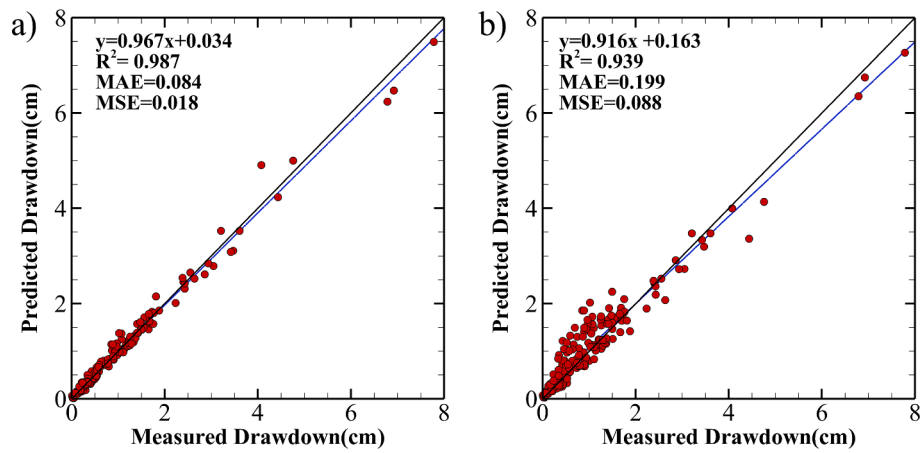


Fig. 10. Scatterplots of the measured versus predicted steady heads of the validation experiments using a) K estimates from SSHT; and b) those based on the visualized layering and the permeameter measured K , respectively.

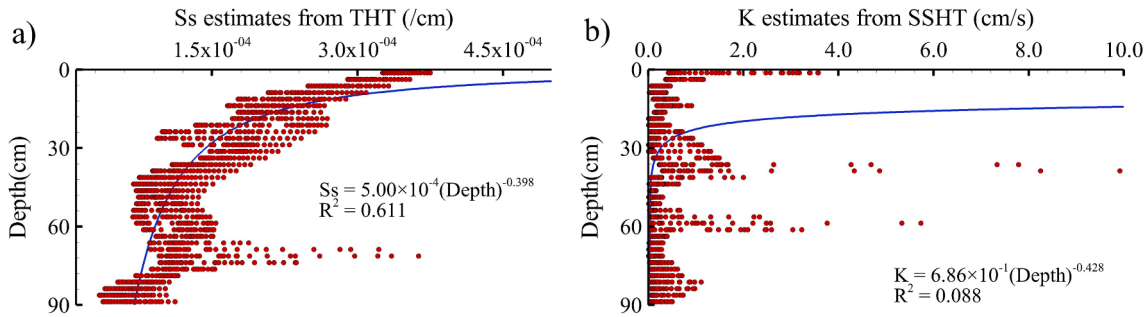


Fig. 11. Relationship a) between S_s estimates from THT and depth; and b) between K estimates from SSHT and depth.

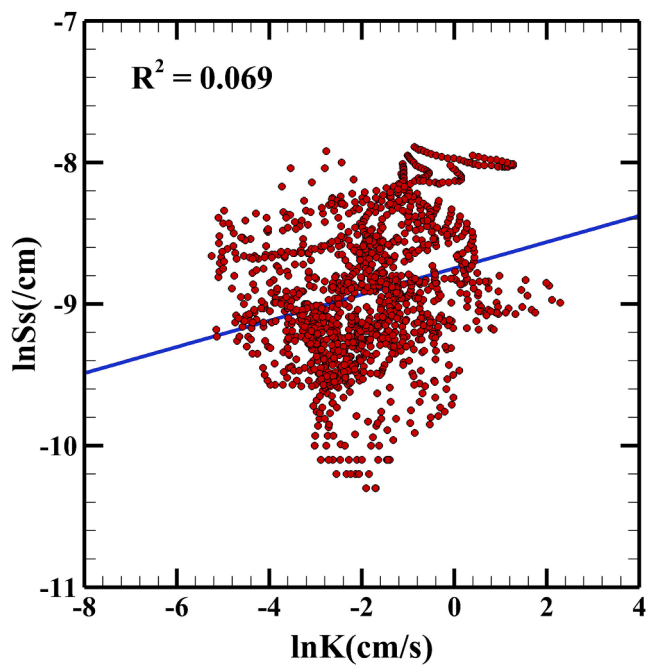


Fig. 12. Scatterplots of $\ln K$ versus $\ln S_s$ estimates fitted to the linear model.

compaction of quartz sand aquifer. However, in the large-scale aquifers, Athy (1930) found that many sandy porous media at 4,000 feet are more porous and less dense than very similar sandy porous media at shallow depths. In other words, changes caused by pressure in sands are minor

compared to changes caused by other factors (e.g., temperature). Chen et al. (2020) proposed a model describing the decreasing trend of n with increasing depth over the range of 0–5 km. Our sandbox aquifer was small, and only had a depth of 90 cm. Thus, the impact of overlying materials stresses on n was insignificant according to Sepúlveda and Zack (1991), Elias and Hajash (1992), and Athy (1930).

Lambe and Whitman (1969) noted that effective stress increases with increasing the overburden stresses. The individual particles move relative to each other to produce a lower void ratio, resulting in the compression and ultimate compaction of the materials. Terzaghi and Peck (1967) and Sharp and Domenico (1976) articulated that when overburden stresses increase, the compressibility of aquifer materials decreases with decreasing S_s . Similarly, Sepúlveda and Zack (1991) noted that the changes in the void ratio of the aquifer matrix over the depth due to overburden stress determine the pore-volume compressibility and matrix permeability at specific depths within aquifers, which in turn supports the depth-dependent profiles of S_s .

S_s estimates obtained from THT analysis show a decreasing trend with depth in sandbox aquifers, and a similar finding has also been reported in sandbox studies from Liu et al. (2007) and Zhao and Illman (2021). If Eq. (11) and the discussion above are valid, the porosity likely does not change with depth in shallow aquifers. The decreasing S_s is likely attributed to the decrease in the medium's compressibility.

The above discussion also supports our result that no clear spatial correlation exists between K and S_s in porous media.

6. Conclusions

This study investigates the spatial correlation between K and S_s in a sandbox aquifer. We first use numerical experiments to verify the robustness of SimSLE for interpreting head data sets from HT surveys to

determine K and S_s fields in two types of heterogeneous aquifers where S_s heterogeneity is correlated and uncorrelated with K heterogeneity. Numerical experiments certify that HT with SimSLE detects the correlation between two heterogeneous fields. Afterward, we conducted HT surveys to depict K and S_s fields in the sandbox, which were validated by predicting drawdowns induced by pumping tests not used in the HT calibration. The sandbox experiment results lead to the following major findings and conclusions:

- (1) HT with SimSLE is a viable technology for mapping K and S_s heterogeneity in aquifers.
- (2) K estimates in the sandbox experiment increase with grain sizes of sands, but no such trend exists in S_s estimates. The distribution of K estimates exhibits the layer structures in the sandbox due to the variation in sand grain sizes, while S_s estimates show unclear layer structures.
- (3) The degree of S_s heterogeneity is much lower than that of K heterogeneity. However, ignoring S_s heterogeneity impairs the prediction of transient behaviors of groundwater flows correctly.
- (4) S_s estimates decrease with the depth in a power-law fashion, while there is no such trend in K estimates, indicating that S_s is more sensitive to overburden stresses than K . A knowledge of decreasing S_s field with depth could improve groundwater flow analyses and groundwater storage assessment in aquifers for groundwater resource management.
- (5) No clear relationship between K and S_s is found. That is, the information about K does not help to estimate S_s .

Lastly, these results are from a small sandbox experiment. The principal findings may be likely valid for field situations but remain to be tested in the fields. We finally echo the call to change how we collect and analyze data, exploiting tomography concepts to characterize aquifers, as [Yeh and Lee \(2007\)](#) advocated.

CRediT authorship contribution statement

Liqun Jiang: Methodology, Writing – original draft, Conceptualization. **Ronglin Sun:** Conceptualization, Supervision, Writing – review & editing. **Wei Xiao:** Data curation. **Xing Liang:** Supervision. **Tian-Chyi Jim Yeh:** Writing – review & editing.

Declaration of Competing Interest

The authors declare that they have no known competing financial interests or personal relationships that could have appeared to influence the work reported in this paper.

Acknowledgments

This research was supported by the National Natural Science Foundation of China (42172286, 41772268). Tian-Chyi Jim Yeh acknowledges the partial support from the U.S. NSF grant EAR1931756. Finally, data and results presented in this manuscript are available at doi:10.5281/zenodo.1435235.

Appendix A. Supplementary data

Supplementary data to this article can be found online at <https://doi.org/10.1016/j.jhydrol.2022.127921>.

References

- Athy, L.F., 1930. Density, porosity and compaction of sedimentary rock. *Ame. Assoc. Petro. Geolo. Bulle.* 14, 1–24. <https://doi.org/10.1306/3D93289E-16B1-11D7-8645000102C1856D>.
- Bear, J., 1972. *Dynamics of Fluids in Porous Media*. Elsevier, New York.
- Beavan, J., Evans, K., Mousa, S., Simpson, D., 1991. Estimating aquifer parameters from analysis of forced fluctuations in well level: an example from the Nubian Formation near Aswan, Egypt: 2. Poroelastic properties. *J. Geophys. Res. Atmos.* 96 (B7), 12139–12160. <https://doi.org/10.1029/91JB00956>.
- Berg, S.J., Illman, W.A., 2011. Three-dimensional transient hydraulic tomography in a highly heterogeneous glaciofluvial aquifer-aquitard system. *Water Resour. Res.* 47, W10507. <https://doi.org/10.1029/2011WR010616>.
- Bohling, G.C., Butler Jr., J.J., Zhan, X., Knoll, M.D., 2007. A field assessment of the value of steady shape hydraulic tomography for characterization of aquifer heterogeneities. *Water Resour. Res.* 43, W05430. <https://doi.org/10.1029/2006WR004932>.
- Brauchler, R., Hu, R., Dietrich, P., Sauter, M., 2011. A field assessment of high-resolution aquifer characterization based on hydraulic travel time and hydraulic attenuation tomography. *Water Resour. Res.* 47, W03503. <https://doi.org/10.1029/2010WR009635>.
- Brauchler, R., Hu, R., Hu, L., Jimenez, S., Bayer, P., Dietrich, P., Ptak, T., 2013. Rapid field application of hydraulic tomography for resolving aquifer heterogeneity in unconsolidated sediments. *Water Resour. Res.* 49 (4), 2013–2024. <https://doi.org/10.1002/wrcr.20181>.
- Bredenhoef, J.D., Belitz, K., Sharp-Hansen, S., 1992. The hydrodynamics of the Big Horn Basin: a study of the role of faults. *AAPG Bull.* 76 (4), 530–546. <https://doi.org/10.1306/BDFF8862-1718-11D7-8645000102C1865D>.
- Cardiff, M., Barrash, W., Kitanidis, P.K., Malama, B., Revil, A., Straface, S., Rizzo, E., 2009. A potential-based inversion of unconfined steady-state hydraulic tomography. *Groundwater* 47 (2), 259–270. <https://doi.org/10.1111/j.1745-6584.2008.00541.x>.
- Cardiff, M., Barrash, W., Kitanidis, P.K., 2012. A field proof-of-concept of aquifer imaging using 3-D transient hydraulic tomography with modular, temporarily-emplaced equipment. *Water Resour. Res.* 48, W05531. <https://doi.org/10.1029/2011WR011704>.
- Castagna, M., Becker, M.W., Bellin, A., 2011. Joint estimation of transmissivity and storativity in a bedrock fracture. *Water Resour. Res.* 47, W09504. <https://doi.org/10.1029/2010WR009262>.
- Chen, J., Kuang, X., Zheng, C., 2020. An empirical porosity–depth model for Earth's crust. *Hydrogeology Journal*, 28: 2331–2339. <https://doi.org/10.1007/s10040-020-02214-x>.
- Chilingarian, G.V., 1983. *Compactional diagenesis*. In: Parker, A., Sellwood, B.W. (Eds.), *Sediment diagenesis*. Reidel, Dordrecht, The Netherlands, pp. 51–167.
- Contoux, C., Violette, S., Vivona, R., Goblet, P., Patriarche, D., 2013. How basin model results enable the study of multi-layer aquifer response to pumping: the Paris Basin, France. *Hydrogeol. J.* 21 (3), 545–557. <https://doi.org/10.1007/s10040-013-0955-6>.
- Cooper Jr., H.H., 1966. The equation of groundwater flow in fixed and deforming coordinates. *J. Geophys. Res. Atmos.* 71 (20), 4785–4790. <https://doi.org/10.1029/JZ071i020p04785>.
- Cooper Jr., H.H., Jacob, C.E., 1946. A generalized graphical method for evaluating formation constants and summarizing well field history. *Eos Trans. Am. Geophys. Union* 27 (4), 526–534. <https://doi.org/10.1029/TR027i004p00526>.
- Dagan, G., 1986. Statistical theory of groundwater flow and transport: Pore to laboratory, laboratory to formation, and formation to regional scale. *Water Resour. Res.* 22 (9), 1203–1245S. <https://doi.org/10.1029/WR022i09Sp0120S>.
- Daranond, K., Yeh, T.-C.J., Hao, Y., Wen, J.-C., Wang, W., 2020. Identification of groundwater basin shape and boundary using hydraulic tomography. *J. Hydrol.* 588, 125099. <https://doi.org/10.1016/j.jhydrol.2020.125099>.
- Elias, B.P., Hajash Jr., A., 1992. Changes in quartz solubility and porosity due to effective stress: an experimental investigation of pressure solution. *Geology* 20, 451–454. [https://doi.org/10.1130/0091-7613\(1992\)020.2.CO;2](https://doi.org/10.1130/0091-7613(1992)020.2.CO;2).
- Eramian, M.G., Schincariol, R.A., Mansinha, L., Stockwell, R.G., 1999. Generation of aquifer heterogeneity maps using two-dimensional spectral texture segmentation techniques. *Math. Geol.* 31 (3), 327–348. <https://doi.org/10.1023/A:1007578305616>.
- Gao, X., Yeh, T.-C.J., Yan, E.-C., Wang, Y.-L., Hao, Y., 2021. Conditional mean, effective, and realizations of hydraulic conductivity fields. *J. Hydrol.* 592, 125606 <https://doi.org/10.1016/j.jhydrol.2020.125606>.
- Gelhar, L.W., 1986. Stochastic subsurface hydrology from theory to applications. *Water Resour. Res.* 22 (9), 135S–145S. <https://doi.org/10.1029/WR022i09Sp0135S>.
- Gelhar, L.W., 1993. Stochastic subsurface hydrology. Prentice hall, p. 390. ISBN: 0138467676.
- Gottlieb, J., Dietrich, P., 1995. Identification of the permeability distribution in soil by hydraulic tomography. *Inverse Prob.* 11 (2), 353–360. <https://doi.org/10.1088/0266-5611/11/2/005>.
- Gutjahr, A.L., 1989. *Fast Fourier Transforms for random field generation: Project Report for Los Alamos Grant to New Mexico Tech*. New Mexico Institute of Mining and Technology.
- Hall, H.N., 1953. Compressibility of reservoir rocks. *J. Petrol. Technol.* 5 (01), 17–19. <https://doi.org/10.2118/953309-G>.
- Hantush, M.S., 1964. Hydraulics of wells. *Adv. Hydrosci.* 1, 281–432. <https://doi.org/10.1016/B978-1-4831-9932-0.50010-3>.
- Hochstetler, D.L., Barrash, W., Leven, C., Cardiff, M., Chidichimo, F., Kitanidis, P.K., 2016. Hydraulic tomography: continuity and discontinuity of high- K and low- K zones. *Groundwater* 54 (2), 171–185. <https://doi.org/10.1111/gwat.12344>.
- Hu, R., Brauchler, R., Herold, M., Bayer, P., 2011. Hydraulic tomography analog outcrop study: Combining travel time and steady shape inversion. *J. Hydrol.* 409 (1–2), 350–362. <https://doi.org/10.1016/j.jhydrol.2011.08.031>.
- Illman, W.A., Liu, X., Takeuchi, S., Yeh, T.-C.J., Ando, K., Saegusa, H., 2009. Hydraulic tomography in fractured granite: Mizunami Underground Research site, Japan. *Water Resour. Res.* 45, W01406. <https://doi.org/10.1029/2007WR006715>.

- Ingebritsen, S.E., Manning, C.E., 2010. Permeability of the continental crust: dynamic variations inferred from seismicity and metamorphism. *Geofluids* 10 (1–2), 193–205. <https://doi.org/10.1111/j.1468-8123.2010.00278.x>.
- Jiang, L., Sun, R., Yeh, T.-C.J., Liang, X., 2021. Inverse modeling of different stimuli and hydraulic tomography: a laboratory sandbox investigation. *J. Hydrol.* 603, 127108. <https://doi.org/10.1016/j.jhydrol.2021.127108>.
- Kell, G.S., 1975. Density, thermal expansivity, and compressibility of liquid water from 0. deg. to 150.deg. Correlations and tables for atmospheric pressure and saturation reviewed and expressed on 1968 temperature scale. *J. Chem. Eng. Data* 20 (1), 97–105. <https://doi.org/10.1021/je60064a005>.
- Kuang, X., Jiao, J.J., Zheng, C., Cherrye, J.A., Li, H., 2020. A review of specific storage in aquifers. *J. Hydrol.* 581, 124383. <https://doi.org/10.1016/j.jhydrol.2019.124383>.
- Lambe, T.W., Whitman, R.V., 1969. *Soil mechanics*. Wiley, New York, p. 553.
- Liu, X., Illman, W.A., Craig, A., Zhu, J., Yeh, T.-C.J., 2007. Laboratory sandbox validation of transient hydraulic tomography. *Water Resour. Res.* 43, W05404. <https://doi.org/10.1029/2006WR005144>.
- Luo, N., Illman, W.A., Zha, Y., Park, Y.-J., Berg, S.J., 2020. Three-dimensional hydraulic tomography analysis of long-term municipal wellfield operations: validation with synthetic flow and solute transport data. *J. Hydrol.* 590, 125438. <https://doi.org/10.1016/j.jhydrol.2020.125438>.
- Manning, C.E., Ingebritsen, S.E., 1999. Permeability of the continental crust: implications of geothermal data and metamorphic systems. *Rev. Geophys.* 37 (1), 127–150. <https://doi.org/10.1029/1998RG900002>.
- Mao, D., Yeh, T.-C.J., Wan, L.i., Hsu, K.-C., Lee, C.-H., Wen, J.-C., 2013. Necessary conditions for inverse modeling of flow through variably saturated porous media. *Adv. Water Resour.* 52, 50–61. <https://doi.org/10.1016/j.advwatres.2012.08.001>.
- Mao, D., Liu, Z., Wang, W., Li, S., Gao, Y., Xu, Z., Zhang, C., 2018. An application of hydraulic tomography to a deep coal mine: Combining traditional pumping tests with water inrush incidents. *J. Hydrol.* 567, 1–11. <https://doi.org/10.1016/j.jhydrol.2018.09.058>.
- Nagelkerke, N.J.D., 1991. A note on a general definition of the coefficient of determination. *Biometrika* 78 (3), 691–692. <https://doi.org/10.1093/biomet/78.3.691>.
- Rao, C.R., 1973. *Linear statistical Inference and Its Applications*, 2nd ed. Wiley, New York.
- Schöniger, A., Nowak, W., Hendricks Franssen, H.-J., 2012. Parameter estimation by ensemble Kalman filters with transformed data: approach and application to hydraulic tomography. *Water Resour. Res.* 48, W04502. <https://doi.org/10.1029/2011WR010462>.
- Sepúlveda, N., Zack, A.L., 1990. Laboratory simulation of the effects of overburden stress on the specific storage of shallow artesian aquifers. Proceedings of the International Symposium on Tropical Hydrology, San Juan, Puerto Rico, *American Water Resources Association*, TPS-90-2: 349–356.
- Sepúlveda, N., Zack, A.L., 1991. The effects of overburden stress on the specific storage and hydraulic conductivity of artesian aquifers. *J. Hydrol.* 128 (1–4), 305–321. [https://doi.org/10.1016/0022-1694\(91\)90144-7](https://doi.org/10.1016/0022-1694(91)90144-7).
- Sharp, J.M., Domenico, P.A., 1976. Energy transport in thick sequences of compacting sediment. *Geological Society of America Bulletin*, 87 (3): 390–400. [https://doi.org/10.1130/0016-7606\(1976\)87<390:ETITS>2.0.CO;2](https://doi.org/10.1130/0016-7606(1976)87<390:ETITS>2.0.CO;2).
- Soueid Ahmed, A., Jardani, A., Revil, A., Dupont, J.P., 2014. Hydraulic conductivity field characterization from the joint inversion of hydraulic heads and self-potential data. *Water Resour. Res.* 50 (4), 3502–3522. <https://doi.org/10.1002/2013WR014645>.
- Sun, R., Yeh, T.-C.J., Mao, D., Jin, M., Lu, W., Hao, Y., 2013. A temporal sampling strategy for hydraulic tomography analysis. *Water Resour. Res.* 49 (7), 3881–3896. <https://doi.org/10.1002/wrcr.20337>.
- Terzaghi, K., Peck, R.B., 1967. *Soil Mechanics in Engineering Practice*, 2nd edn., Wiley, New York, p. 729 pp.
- Tiedeman, C.R., Barrash, W., 2020. Hydraulic tomography: 3D hydraulic conductivity, fracture network, and connectivity in mudstone. *Groundwater* 58 (2), 238–257. <https://doi.org/10.1111/gwat.12915>.
- Tso, C.-H.-M., Zha, Y., Yeh, T.-C.J., Wen, J.-C., 2016. The relative importance of head, flux, and prior information in hydraulic tomography analysis. *Water Resour. Res.* 52 (1), 3–20. <https://doi.org/10.1002/2015WR017191>.
- Van der Kamp, G., Gale, J.E., 1983. Theory of earth tide and barometric effects in porous formations with compressible grains. *Water Resour. Res.* 19 (2), 538–544. <https://doi.org/10.1029/WR19i002p00538>.
- Wen, J.-C., Chen, J.-L., Yeh, T.-C.J., Wang, Y.-L., Huang, S.-Y., Tian, Z., Yu, C.-Y., 2019. Redundant and nonredundant information for model calibration or hydraulic tomography. *Groundwater* 58 (1), 79–92. <https://doi.org/10.1111/gwat.12879>.
- Wu, C.-M., Yeh, T.-C.J., Zhu, J., Lee, T.H., Hsu, N.-S., Chen, C.-H., Sancho, A.F., 2005. Traditional analysis of aquifer tests: Comparing apples to oranges? *Water Resour. Res.* 41, W09402. <https://doi.org/10.1029/2004WR003717>.
- Xiang, J., Yeh, T.-C.J., Lee, C.-H., Hsu, K.-C., Wen, J.-C., 2009. A simultaneous successive linear estimator and a guide for hydraulic tomography analysis. *Water Resour. Res.* 45, W02432. <https://doi.org/10.1029/2008WR007180>.
- Xu, D., Sun, R., Yeh, T.-C.J., Wang, Y.-L., Momayez, M., Hao, Y., Lee, C.-H., Hu, X., 2019. Mapping soil layers using electrical resistivity tomography and validation: sandbox experiments. *J. Hydrol.* 575, 523–536. <https://doi.org/10.1016/j.jhydrol.2019.05.036>.
- Yeh, T.-C.J., Jin, M., Hanna, S., 1996. An iterative stochastic inverse method: conditional effective transmissivity and hydraulic head fields. *Water Resour. Res.* 32 (1), 85–92. <https://doi.org/10.1029/95WR02869>.
- Yeh, T.-C.J., Khaleel, R., Carroll, K.C. (Eds.), 2015. *Flow Through Heterogeneous Geologic Media*. Cambridge University Press, Cambridge. ISBN: 9781107076136.
- Yeh, T.-C.J., Lee, C.-H., 2007. Time to change the way we collect and analyze data for aquifer characterization. *Groundwater* 45 (2), 116–118. <https://doi.org/10.1111/j.1745-6584.2006.00292.x>.
- Yeh, T.-C.J., Liu, S., 2000. Hydraulic tomography: Development of a new aquifer test method. *Water Resour. Res.* 36 (8), 2095–2105. <https://doi.org/10.1029/2000WR000114>.
- Yeh, T.-C.J., Srivastava, R., Guzman, A., Harter, T., 1993. A numerical model for water flow and chemical transport in variably saturated porous media. *Groundwater* 31 (4), 634–644. <https://doi.org/10.1111/j.1745-6584.1993.tb00597.x>.
- Zha, Y., Yeh, T.-C.J., Illman, W.A., Tanaka, T., Bruines, P., Onoe, H., Saegusa, H., 2015. What does hydraulic tomography tell us about fractured geological media? A field study and synthetic experiments. *J. Hydrol.* 531 (1), 17–30. <https://doi.org/10.1016/j.jhydrol.2015.06.013>.
- Zhao, Z., Illman, W.A., 2021. On the importance of considering specific storage heterogeneity in hydraulic tomography: Laboratory sandbox and synthetic studies. *J. Hydrol.* 593, 125874. <https://doi.org/10.1016/j.jhydrol.2020.125874>.
- Zhu, J., Yeh, T.-C.J., 2005. Characterization of aquifer heterogeneity using transient hydraulic tomography. *Water Resour. Res.* 41, W07028. <https://doi.org/10.1029/2004WR003790>.